

A Semantically Disentangled Unified Model for Multi-category 3D Anomaly Detection

SuYeon Kim Wongyu Lee MyeongAh Cho[†]
 Kyung Hee University, Republic of Korea
 {spoiuy3, fovert, maycho}@khu.ac.kr

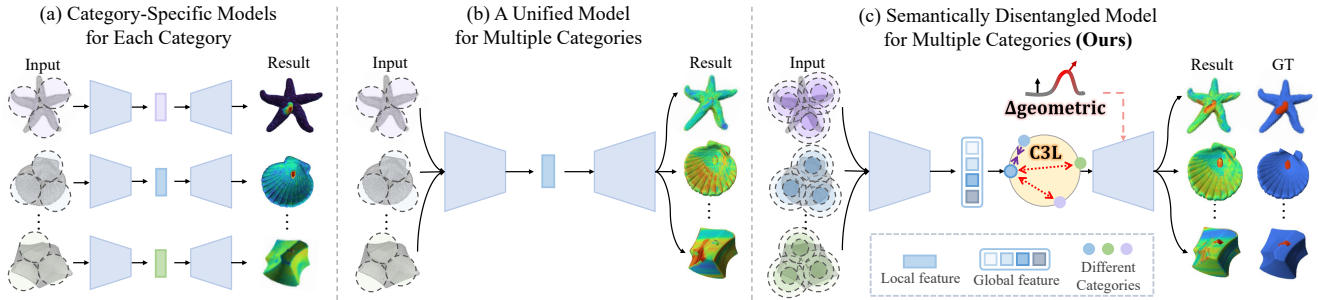


Figure 1. Overview of different paradigms for 3D anomaly detection. (a) Category-specific models trained on each object class separately. (b) A unified model handles multiple categories with local features but often suffers from inter-category feature entanglement. (c) Our method achieves semantically consistent results by aggregating coarse-to-fine geometric cues into category-aware global features, disentangling them via C3L, and guiding reconstruction with input geometry.

Abstract

3D anomaly detection targets the detection and localization of defects in 3D point clouds trained solely on normal data. While a unified model improves scalability by learning across multiple categories, it often suffers from **Inter-Category Entanglement (ICE)**—where latent features from different categories overlap, causing the model to adopt incorrect semantic priors during reconstruction and ultimately yielding unreliable anomaly scores. To address this issue, we propose the **Semantically Disentangled Unified Model** for 3D Anomaly Detection, which reconstructs features conditioned on disentangled semantic representations. Our framework consists of three key components: (i) **Coarse-to-Fine Global Tokenization** for forming instance-level semantic identity, (ii) **Category-Conditioned Contrastive Learning** for disentangling category semantics, and (iii) a **Geometry-Guided Decoder** for semantically consistent reconstruction. Extensive experiments on Real3D-AD and Anomaly-ShapeNet demonstrate that our method achieves state-of-the-art for both unified and category-specific models, improving object-level AUROC by 2.8% and 9.1%, respectively, while enhancing the reliability of unified 3D anomaly detection. Project page: <https://spoiuy3.github.io/SeDiR/>

[†] Corresponding author

1. Introduction

3D anomaly detection (3D-AD) aims to identify defective objects and localize abnormal regions within 3D point clouds, typically trained using only normal data. Conventional methods [16, 19, 45, 46] are category-specific, where a separate model is trained for each object type (Fig. 1 (a)). These models—most commonly based on encoder-decoder reconstruction or memory matching—learn the normal pattern distribution of a single category. During inference, reconstruction-based methods detect anomalies when the model fails to reconstruct an abnormal sample, whereas memory-based approaches identify anomalies when the feature representation of an abnormal sample deviates significantly from the stored normal patterns. Although effective under controlled conditions, this paradigm has two major limitations. First, it suffers from **transfer collapse**—the model becomes overly specialized to a specific geometric pattern of normal training samples and fails to generalize over shape or texture variations. Second, it is **impractical in real industrial scenarios** involving multiple object categories, as it requires duplicating training, storage, and maintenance pipelines for each class. To address these constraints, a recent study [3] has explored unified 3D-AD framework, where a single model is jointly trained across multiple categories (Fig. 1 (b)). Such unified design reduces system redundancy and improves deployment effi-

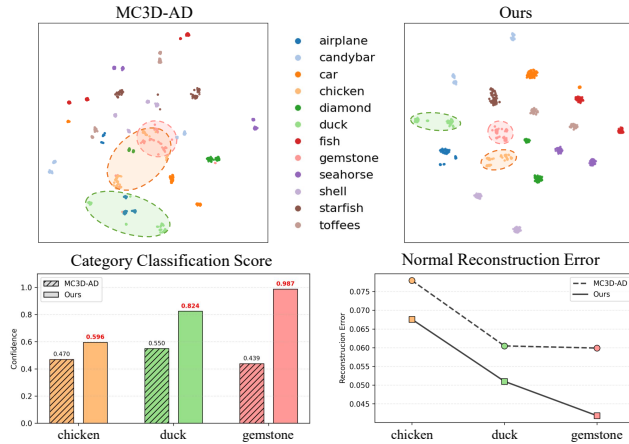


Figure 2. T-SNE visualization and quantitative analysis of semantic disentanglement. MC3D-AD exhibits entangled feature clusters across similar categories (e.g., *chicken*, *duck*, *gemstone*), where samples with low category classification scores are reconstructed under uncertain semantic priors, yielding high reconstruction errors on normal data and increased false positives. Our model instead forms well-separated, semantically aligned manifolds with higher classification scores and lower reconstruction errors, enabling reliable category-conditioned reconstruction.

ciency, emerging as a promising direction for practical 3D anomaly detection.

A unified model offers improved practicality and even higher accuracy, yet a critical question remains—**can a model truly detect anomalies without first establishing an object’s identity?** In unified 3D-AD, the model is expected to learn normal shape priors across multiple categories and detect anomalies through reconstruction errors. However, our observations reveal a deeper issue: even when trained only on normal data, the model sometimes reconstructs objects using the wrong category prior (e.g., a chair partially reconstructed with table-like geometry). This does not indicate a failure to detect anomalies, but rather a failure to establish the object’s identity before reconstruction. We define this phenomenon as **Inter-Category Entanglement (ICE)**—a state in which features from different categories become entangled in the latent space, preventing the formation of distinct, category-specific representations. When the ICE problem occurs, the model loses semantic identity, and reconstruction is guided by an incorrect category prior. This semantic misalignment propagates through the entire pipeline, leading to geometrically inconsistent outputs and degraded performance in both anomaly detection and localization.

To validate the presence of the ICE problem, in Fig. 2, we perform both qualitative and quantitative analyses using MC3D-AD [3]. We first project encoder features into t-SNE space [23] and observe that categories such as *chicken*, *duck*, and *gemstone* form heavily overlapping clusters rather than distinct manifolds. Furthermore, to quantify the cate-

gory classification score, we freeze the trained model and train a lightweight MLP on the reconstructed features. By analyzing the relationship between the classification score and the reconstruction error on normal test samples, we observe that samples with low semantic score tend to exhibit significantly higher reconstruction errors. These observations confirm that incorrect semantic understanding leads to incorrect reconstruction, demonstrating that the ICE problem is not a random side effect but a systematic bottleneck in unified 3D-AD.

The above observations indicate that the fundamental limitation of unified 3D-AD is not the difficulty of reconstructing anomalies, but the attempt to reconstruct before understanding what is being reconstructed. In other words, reconstruction fails not because the object is anomalous, but because the model lacks a clear semantic identity of the object in the first place. This misalignment—where geometry is reconstructed under an incorrect category prior—leads to unreliable anomaly scores and mislocalized defects. Therefore, we reformulate unified 3D-AD as a problem of **semantically conditioned reconstruction** and propose the paradigm of **Semantically Disentangled Reconstruction** (Fig. 1 (c)), where reconstruction is conditioned on correctly disentangled, category-level semantics rather than indiscriminately applied to all latent representations.

To operationalize Semantically Disentangled Reconstruction, we design a semantically disentangled unified framework, named **SeDiR**, that explicitly separates semantic identity from geometry before attempting reconstruction. We propose the **Coarse-to-Fine Global Tokenization (CFGT)** module, which aggregates multi-resolution geometric cues into a global token that captures category-aware semantics rather than relying solely on local point features. This global representation enables the model to form a reliable semantic identity of the object before any decoding takes place. To further prevent different categories from collapsing into a shared latent space, we introduce **Category-Conditioned Contrastive Learning (C3L)**, which explicitly enforces intra-category compactness and inter-category separation to form distinct semantic manifolds, directly mitigating Inter-Category Entanglement. Finally, we propose a **Geometry-Guided Decoder (GGD)** that performs reconstruction guided by both the disentangled semantic prior and local geometric evidence. Instead of decoding blindly from latent features, the decoder is softly biased towards category-consistent reconstruction pathways, ensuring that geometry is reconstructed according to the correct semantic identity. Together, these components enable the model to understand *what* it is reconstructing before deciding *how* to reconstruct, establishing a new perspective and solution space for unified 3D anomaly detection. Extensive experiments validate the effectiveness of our framework, showing consistent improvements and outperforming both category-

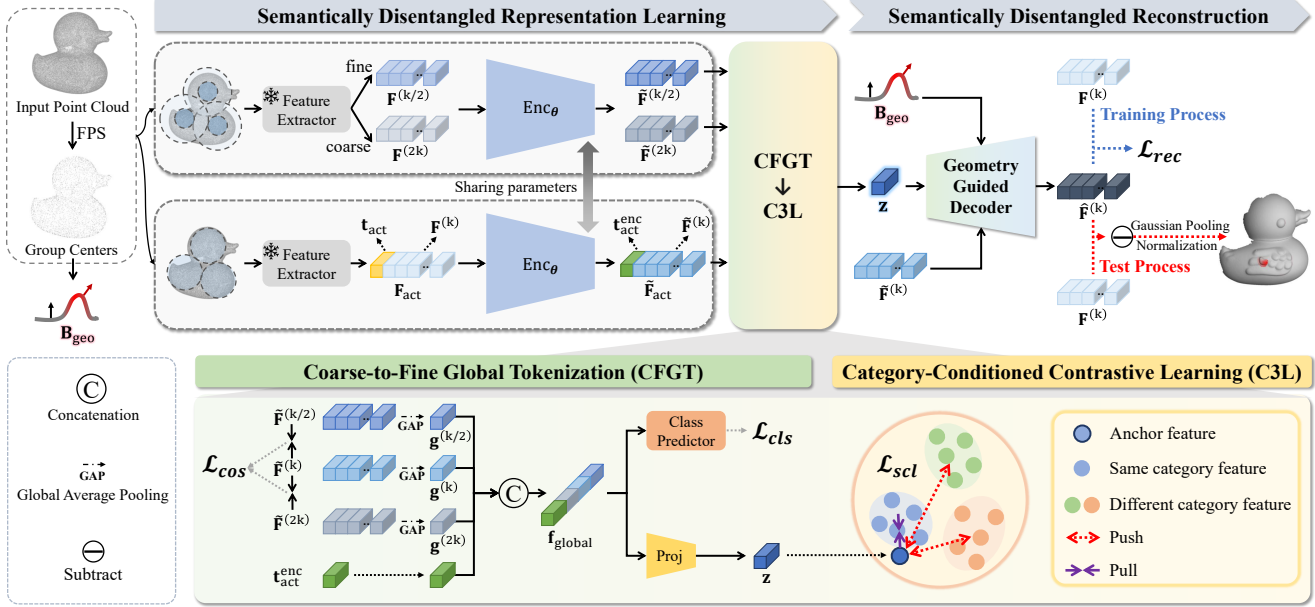


Figure 3. **The overview of the proposed method.** Our method consists of two main stages: Semantically Disentangled Representation Learning and Semantically Disentangled Reconstruction. Given an input point cloud, CFGT encodes multi-resolution geometric features into a category-aware global token, C3L disentangles the latent semantics, and GGD reconstructs the object conditioned on these disentangled semantics and geometric priors.

specific and unified state-of-the-art baselines by 2.8% and 9.1% in object-level AUROC on Real3D-AD and Anomaly-ShapeNet, respectively.

2. Related Works

2.1. 2D Anomaly Detection

Unsupervised 2D image-based anomaly detection (2D-AD) has advanced rapidly in recent years, mainly through two paradigms: feature-embedding and reconstruction-based methods. Feature-embedding methods model the latent distribution of normal data using pretrained representations and detect anomalies by measuring the distance from the normal feature manifold [4, 28, 29, 31, 40]. Reconstruction-based approaches train generative models such as autoencoders [13, 20, 27, 30, 42], GANs [6, 18, 35], transformers [14, 25, 36], or diffusion models [7, 10, 34, 37] to reconstruct normal images and use the reconstruction error as the anomaly score. Recently, unified frameworks have been proposed to replace class-specific models, enabling generalization across categories [8, 9, 22, 38, 41, 44]. Some of these methods [5, 33] employ contrastive learning to structure feature spaces with clearer inter-class boundaries. However, these approaches focus solely on semantic separation in 2D feature space and lack explicit mechanisms for geometric consistency, making direct extension to 3D data difficult.

2.2. 3D Anomaly Detection

Research on 3D-AD with point clouds has accelerated in recent years. Existing approaches are broadly grouped into memory bank-based and reconstruction-based methods. Memory bank-based methods store features of normal point clouds and compare test samples using similarity metrics [17, 19, 46]. Reconstruction-based methods instead learn to reproduce normal shapes and identify anomalies through reconstruction errors [16, 45]. Similar to 2D-AD, unified 3D-AD framework has recently emerged to enable anomaly detection across multiple categories within a single model. MC3D-AD [3] aims to generalize across categories but often suffers from *inter-category entanglement (ICE)*, where features from different classes interfere with one another. This highlights the need for disentangling category-specific semantics while preserving geometric consistency—a challenge our method directly addresses.

3. Method

Problem statement. Let $\mathcal{C} = \{1, \dots, C\}$ be the set of object categories. For each category $c \in \mathcal{C}$, we denote the training set by $\mathcal{D}_{\text{train}}^c = \{P_q^c\}_{q=1}^{M_c}$, where each point cloud $P_q^c \in \mathbb{R}^{N \times 3}$ contains N points, and M_c is the number of training samples. The corresponding test set is given by $\mathcal{D}_{\text{test}}^c = \{(P_q^c, t_q^c)\}_{q=1}^{T_c}$, where $t_q^c \in \mathcal{T} := \{0, 1\}$ indicates whether the sample is normal (0) or anomalous (1). For the multi-category 3D anomaly detection setting, we construct

unified datasets across all categories as $\mathcal{D}_{\text{train}} = \bigcup_{c=1}^C \mathcal{D}_{\text{train}}^c$ and $\mathcal{D}_{\text{test}} = \bigcup_{c=1}^C \mathcal{D}_{\text{test}}^c$. The goal of this task is to train a unified model using only normal samples from $\mathcal{D}_{\text{train}}$, and evaluate it on object-level anomaly detection and point-level anomaly localization.

Overview. The overview of our framework **SeDiR** is illustrated in Fig. 3. Given an input point cloud, multi-resolution geometric features are extracted via a shared encoder, where a learnable token \mathbf{t}_{act} is appended to capture instance-level contextual information. These feature sequences are processed by the CFGT to generate a category-aware global token and are further optimized with C3L to achieve semantically disentangled feature separation. The GGD then reconstructs feature tokens in a semantically consistent manner, conditioned on both the global token and geometric bias guided by the input geometry. During inference, reconstruction errors are aggregated using Gaussian pooling and normalization to compute the final anomaly score. The details of each component are described in the following sections.

3.1. Coarse-to-Fine Global Tokenization

Multi-resolution neighborhood encoding. Given a point cloud $\mathbf{P} = \{\mathbf{p}_n\}_{n=1}^N$, $\mathbf{p}_n \in \mathbb{R}^3$, we first select g centers $\mathcal{S} = \{\mathbf{s}_m\}_{m=1}^g$ via Farthest Point Sampling (FPS) [26]. Based on a base neighborhood size k , we define a set of symmetric resolutions $\mathcal{R} = \{k/2, k, 2k\}$ to capture both fine- and coarse-scale geometric context. For each $r \in \mathcal{R}$, Euclidean neighborhoods are constructed around the shared centers \mathcal{S} using the k -nearest neighbors (kNN) algorithm, and each neighborhood is encoded using a pretrained local encoder $E(\cdot)$ (e.g., PointMAE [24]):

$$\mathcal{N}_r(\mathbf{s}_m) = \text{kNN}(\mathbf{s}_m; r), \quad \mathbf{f}_m^{(r)} = E(\mathcal{N}_r(\mathbf{s}_m)) \in \mathbb{R}^d. \quad (1)$$

Smaller neighborhoods ($k/2$) focus on fine details, while larger ones ($2k$) encode broader structural context. Collectively, these multi-resolution neighborhoods capture complementary geometric cues across scales, forming a coarse-to-fine representation. Finally, the resulting feature tokens across all centers are aggregated into a resolution-specific feature sequence:

$$\mathbf{F}^{(r)} = [\mathbf{f}_1^{(r)}, \dots, \mathbf{f}_g^{(r)}] \in \mathbb{R}^{g \times d}. \quad (2)$$

Additional experiments exploring various symmetric resolution configurations are included in the supplementary.

Instance-level global representation via adaptive context token. Although multi-resolution encoding captures geometry, it lacks an instance-level semantic representation. To construct such a global representation, we introduce a learnable *Adaptive Context Token* (ACT), denoted as $\mathbf{t}_{\text{act}} \in \mathbb{R}^{1 \times d}$, and prepend it to the base-resolution feature sequence, forming $\mathbf{F}_{\text{act}} = \text{concat}([\mathbf{t}_{\text{act}}, \mathbf{F}^{(k)}]) \in \mathbb{R}^{(g+1) \times d}$. The ACT dynamically aggregates global context. A transformer encoder ENC_θ with shared weights processes both

the coarse-to-fine sequences and the ACT-augmented base sequence:

$$\tilde{\mathbf{F}}^{(r)} = \text{ENC}_\theta(\mathbf{F}^{(r)}), \quad \tilde{\mathbf{F}}_{\text{act}} = \text{ENC}_\theta(\mathbf{F}_{\text{act}}), \quad (3)$$

where $r \in \{k/2, 2k\}$. The output of $\tilde{\mathbf{F}}_{\text{act}}$ excluding the ACT corresponds to the base-resolution feature sequence $\tilde{\mathbf{F}}^{(k)}$.

To encourage cross-scale consistency, we impose a cosine alignment loss between the base tokens and their fine- and coarse-scale counterparts:

$$\mathcal{L}_{\text{cos}} = \frac{1}{g} \sum_{m=1}^g \sum_{r \in \{k/2, 2k\}} \left[1 - \cos(\tilde{\mathbf{f}}_m^{(k)}, \tilde{\mathbf{f}}_m^{(r)}) \right], \quad (4)$$

where $\cos(\cdot, \cdot)$ denotes the normalized dot product.

To facilitate cross-scale fusion, we summarize the contextual information of each feature sequence via global average pooling, $\mathbf{g}^{(r)} = \text{GlobalAveragePool}(\tilde{\mathbf{F}}^{(r)})$, where $r \in \{k/2, k, 2k\}$, and directly extract the encoded ACT token as $\mathbf{t}_{\text{act}}^{\text{enc}} = \tilde{\mathbf{F}}_{\text{act}}[1, :]$. Finally, we obtain the holistic global representation by concatenating the pooled fine-, base-, and coarse-level features together with the ACT token:

$$\mathbf{f}_{\text{global}} = \text{concat}([\mathbf{g}^{(k)}, \mathbf{g}^{(2k)}, \mathbf{g}^{(k/2)}, \mathbf{t}_{\text{act}}^{\text{enc}}]), \quad (5)$$

which serves as a unified global representation encapsulating both geometric structure and semantic identity. Further analysis on ACT behavior is in the supplementary.

Auxiliary category classification loss. To imbue the global embedding with category awareness, we introduce an auxiliary classification head that predicts the object category as $\hat{\mathbf{y}} = \text{Cls}(\mathbf{f}_{\text{global}})$. Let $\mathbf{y} \in \{0, 1\}^C$ denote the one-hot label for category $c \in \{1, \dots, C\}$. The auxiliary objective is formulated as a standard cross-entropy loss:

$$\mathcal{L}_{\text{cls}} = \text{CrossEntropy}(\hat{\mathbf{y}}, \mathbf{y}). \quad (6)$$

This auxiliary supervision promotes category-aware representations, facilitating semantic disentanglement.

Global token embedding. For each instance, the aggregated global representation $\mathbf{f}_{\text{global}}$ —which encodes both geometric structure and category-aware semantics—is projected through a lightweight head $\text{Proj}(\cdot)$ and subsequently ℓ_2 -normalized to form a compact global token:

$$\mathbf{z} = \text{Proj}(\mathbf{f}_{\text{global}}), \quad \mathbf{z} \in \mathbb{R}^{d_z}, \quad \mathbf{z} = \frac{\mathbf{z}}{\|\mathbf{z}\|_2}. \quad (7)$$

The projector is a two-layer MLP with LayerNorm [1] and GeLU [11], outputting an embedding of dimension d_z . The resulting normalized global token serves as a compact instance descriptor and is further utilized in Sec. 3.2 and Sec. 3.3.

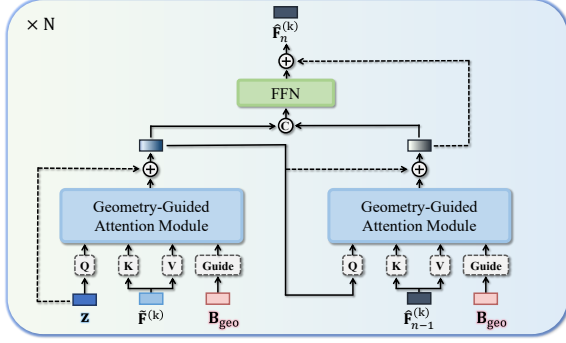


Figure 4. Overview of the Geometry-Guided Decoder (GGD). Geometric priors \mathbf{B}_{geo} guide the attention mechanism to refine semantic features, and the results are aggregated through a feed-forward network.

3.2. Category-Conditioned Contrastive Learning

To mitigate *inter-category entanglement (ICE)*, we propose Category-Conditioned Contrastive Learning (C3L), which further refines the latent space built upon the category-aware global token from CFGT. We construct a dynamic buffer $\mathcal{B} = \{(\mathbf{z}_j, c_j) \mid j = 1, \dots, L\}$ to ensure stable and diverse contrastive samples, where $c_j \in \{1, \dots, C\}$ denotes the category label. We set L to 64, and additional analysis on buffer size sensitivity is provided in the supplementary. For a given embedding \mathbf{z}_i with category c_i , we define its positive and negative sets as $\mathcal{P}(i) = \{\mathbf{z}_{pos} \in \mathcal{B} \mid c_p = c_i\}$, $\mathcal{N}(i) = \{\mathbf{z}_{neg} \in \mathcal{B} \mid c_n \neq c_i\}$, and $\mathcal{A}(i) = \mathcal{P}(i) \cup \mathcal{N}(i)$. Following the supervised contrastive learning formulation [15], the per-sample supervised contrastive loss is formulated as:

$$\mathcal{L}_{\text{scl}}(i) = \frac{1}{|\mathcal{P}(i)|} \sum_{\mathbf{z}_{pos} \in \mathcal{P}(i)} -\log \frac{\exp(\mathbf{z}_i^\top \mathbf{z}_{pos} / \tau)}{\sum_{\mathbf{z}_a \in \mathcal{A}(i)} \exp(\mathbf{z}_i^\top \mathbf{z}_a / \tau)}, \quad (8)$$

where τ denotes the temperature parameter.

Training objective. The final C3L objective combines the supervised contrastive loss, the auxiliary category classification term, and the cross-scale cosine alignment term:

$$\mathcal{L}_{\text{C3L}} = \lambda_{\text{scl}} \mathcal{L}_{\text{scl}} + \lambda_{\text{cls}} \mathcal{L}_{\text{cls}} + \lambda_{\text{cos}} \mathcal{L}_{\text{cos}}, \quad (9)$$

where λ_{scl} , λ_{cls} , and λ_{cos} balance the respective objectives. This joint optimization disentangles inter-category embeddings while preserving compact intra-category geometry, ultimately yielding a semantically disentangled and category-coherent latent space.

3.3. Geometry-Guided Decoder

While CFGT and C3L establish semantically disentangled representations, the final stage of the proposed paradigm translates these category-aware priors into geometrically consistent reconstructions. To this end, we introduce the Geometry-Guided Decoder (GGD), which reconstructs feature tokens conditioned on both the semantic prior and the input geometry.

Let \mathbf{z} denote the global semantic prior and $\tilde{\mathbf{F}}^{(k)} = [\tilde{\mathbf{f}}_1^{(k)}, \dots, \tilde{\mathbf{f}}_g^{(k)}]$ be the encoded k -resolution feature sequence. In GGD, \mathbf{z} serves as the *query* while $\tilde{\mathbf{F}}^{(k)}$ provides the *keys* and *values*. To ensure semantically consistent reconstruction, we incorporate geometric cues directly into the attention mechanism by introducing a geometry-derived bias \mathbf{B}_{geo} , which encodes local geometric variations such as surface normal and curvature changes between point neighborhoods. This bias is added to the attention logits to guide:

$$\text{Attention}(\mathbf{Q}, \mathbf{K}, \mathbf{V}) = \text{softmax} \left(\frac{\mathbf{Q}\mathbf{K}^\top}{\sqrt{d}} + \beta \mathbf{B}_{\text{geo}} \right) \mathbf{V}, \quad (10)$$

where β controls the strength of geometric guidance. Details of \mathbf{B}_{geo} are provided in the supplementary.

As shown in Fig. 4, outputs from two such modules are concatenated and refined via a feed-forward network (FFN) to yield reconstructed feature tokens $\hat{\mathbf{F}}^{(k)} = [\hat{\mathbf{f}}_1^{(k)}, \dots, \hat{\mathbf{f}}_g^{(k)}]$. Reconstruction is supervised by an MSE loss:

$$\mathcal{L}_{\text{rec}} = \frac{1}{g} \sum_{j=1}^g \|\hat{\mathbf{f}}_j^{(k)} - \mathbf{f}_j^{(k)}\|_2^2. \quad (11)$$

Final training objective. The overall objective combines semantic disentanglement and geometry-guided reconstruction:

$$\mathcal{L}_{\text{total}} = \mathcal{L}_{\text{C3L}} + \mathcal{L}_{\text{rec}}, \quad (12)$$

where \mathcal{L}_{C3L} (Eq. (9)) enforces category-conditioned separation and \mathcal{L}_{rec} ensures geometric fidelity. This joint optimization produces reconstructions that are both semantically consistent and geometrically accurate, fulfilling the goal of Semantically Disentangled Reconstruction.

3.4. Anomaly Scoring

At inference, a test point cloud is encoded into feature tokens and reconstructed by the decoder. To quantify the reconstruction discrepancy, we compute the ℓ_2 distance between the original and reconstructed tokens and normalize it within each instance:

$$\mathbf{S}_p = \text{Gauss}_{k_g, \sigma} \left(\text{Norm}(\|\hat{\mathbf{F}}^{(k)} - \mathbf{F}^{(k)}\|_2) \right), \quad (13)$$

where Norm denotes min-max normalization and $\text{Gauss}_{k_g, \sigma}$ is a discrete 1D Gaussian filter applied along the token dimension. The per-point scores \mathbf{S}_p indicate local inconsistencies, and the object-level anomaly score is defined as $S_{\text{obj}} = \max(\mathbf{S}_p)$.

4. Experiments

4.1. Experimental Settings

Datasets. We evaluate our approach on two benchmark datasets: Real3D-AD [19] and Anomaly-ShapeNet [16].

Table 1. Quantitative comparison of AUROC (%) at the object levels on Real3D-AD across 12 categories. The best and second-best results are highlighted in **bold** and underline, respectively. Methods in the upper block are trained and evaluated in the single-category setting, while methods in the lower block use a unified model for the multi-category setting across all 12 categories.

O-AUROC(↑)													
Method	Airplane	Car	Candybar	Chicken	Diamond	Duck	Fish	Gemstone	Seahorse	Shell	Starfish	Toffees	Mean
<i>Category-Specific Method</i>													
BTF(Raw)	73.0	64.7	53.9	78.9	70.7	69.1	60.2	<u>68.6</u>	59.6	39.6	53.0	70.3	63.5
BTF(FPFH)	52.0	56.0	63.0	43.2	54.5	78.4	54.9	64.8	<u>77.9</u>	75.4	57.5	46.2	60.3
M3DM	43.4	54.1	55.2	68.3	60.2	43.3	54.0	64.4	49.5	69.4	55.1	45.0	59.4
PatchCore(FPFH)	88.2	59.0	54.1	<u>83.7</u>	57.4	54.6	67.5	37.0	50.5	58.9	44.1	56.5	59.3
PatchCore(PointMAE)	72.6	49.8	66.3	82.7	78.3	48.9	63.0	37.4	53.9	50.1	51.9	58.5	59.4
CPMF	70.1	55.1	55.2	50.4	52.3	58.2	55.8	58.9	72.9	65.3	70.0	39.0	58.6
IMRNet	76.2	71.1	75.5	78.0	90.5	51.7	88.0	67.4	60.4	66.5	67.4	77.4	72.5
Reg3D-AD	71.6	69.7	68.5	85.2	90.0	58.4	91.5	41.7	76.2	58.3	50.6	82.7	70.4
Group3AD	74.4	<u>72.8</u>	<u>84.7</u>	78.6	<u>93.2</u>	67.9	97.6	53.9	84.1	58.5	56.2	<u>79.6</u>	75.1
R3D-AD	77.2	69.6	71.3	71.4	68.5	90.9	69.2	66.5	72.0	84.0	<u>70.1</u>	70.3	73.4
ISMP	<u>85.8</u>	73.1	85.2	71.4	94.8	71.2	<u>94.5</u>	46.8	72.9	62.3	66.0	84.2	76.7
PO3AD	80.4	65.4	78.5	68.6	80.1	<u>82.0</u>	85.9	69.3	75.6	<u>80.0</u>	75.8	77.1	<u>76.5</u>
<i>Unified Method</i>													
MC3D-AD	85.0	<u>74.9</u>	83.0	<u>71.5</u>	95.5	<u>83.1</u>	<u>86.5</u>	<u>56.0</u>	71.6	80.3	76.6	<u>73.8</u>	<u>78.2</u>
SeDiR (Ours)	86.0	78.3	<u>81.9</u>	72.9	<u>94.8</u>	86.2	93.8	62.7	<u>67.4</u>	<u>77.9</u>	85.4	84.5	81.0

Anomaly-ShapeNet is a synthetic 3D anomaly detection dataset containing 1,600 samples across 40 categories, with 4 normal samples per category in the training set. Real3D-AD is a high-resolution real-world dataset with 12 categories, each with 4 normal training samples and 100 test samples. While both datasets employ complete (360°) point clouds for training, Real3D-AD provides single-view test scans, making anomaly detection more challenging.

Evaluation metrics. Following prior work [16, 19], we evaluate anomaly detection performance using the Area Under the Receiver Operating Characteristic Curve (AUROC). We report O-AUROC for object-level anomaly detection and P-AUROC for point-level anomaly localization. Higher O-AUROC and P-AUROC indicate better detection and localization performance, respectively.

Baseline methods. We compare our method against state-of-the-art approaches, including BTF [12], M3DM [32], PatchCore [28], CPMF [2], IMRNet [16], Reg3D-AD [19], Group3AD [46], R3D-AD [45], ISMP [17], PO3AD [39], and MC3D-AD [3]. MC3D-AD trains a unified model for all categories, while the remaining methods train individual models per category. The results of these methods are obtained from publicly available code or their papers.

4.2. Comparison Results with SOTA Methods

Object-level results on Real3D-AD. As shown in Tab. 1, our method achieves state-of-the-art performance on O-AUROC, outperforming the second-best approach by 2.8% across both single- and multi-category settings. This consistent improvement indicates that our framework effectively learns category-disentangled features, leading to robust 3D anomaly detection across diverse category distributions.

Object-level results on Anomaly-ShapeNet. Tab. 2 reports the object-level AUROC results on the Anomaly-ShapeNet dataset. Our method achieves 93.3% O-AUROC, surpassing the second-best approach by 9.1%. These results demonstrate that discriminative, category-aware representations substantially improve generalization in the unified multi-category setting, enabling more accurate and semantically consistent anomaly detection and localization.

Point-level results. As reported in Tab. 3, our method achieves the second-best P-AUROC on both Real3D-AD and Anomaly-ShapeNet datasets, while single-category approaches exhibit dataset-specific strengths. ISMP [17], a memory-based method, performs best on Real3D-AD by effectively recalling detailed local patterns in real-world data, but its reliance on memorized normal features limits its generalization to synthetic domains (*e.g.*, Anomaly-ShapeNet). PO3AD [39], which generates pseudo-anomalies for supervision, achieves strong results on the synthetic Anomaly-ShapeNet dataset but struggles to generalize to real-world geometries in Real3D-AD. In contrast, our framework maintains consistently high performance across both datasets, demonstrating superior robustness and generalization under the unified multi-category setting.

4.3. Ablation Studies

We perform comprehensive ablation experiments to quantify the contribution of each proposed component to the performance of our model. These are shown across Tab. 4 through Tab. 7.

Effect of each component. Tab. 4 demonstrates the impact of the three proposed modules: CFGT, C3L, and GGD. Incorporating CFGT yields a slight performance gain, as fus-

Table 2. Comparison of object-level AUROC (%) of various methods on the Anomaly-ShapeNet.

O-AUROC(↑)																					
Method	ashtray0	bag0	bottle0	bottle1	bottle3	bow10	bow11	bow12	bow13	bow14	bow15	bucket0	bucket1	cap0	cap3	cap4	cap5	cup0	cup1	eraser0	
<i>Category-Specific Method</i>																					
BTF(Raw)	57.8	41.0	59.7	51.0	56.8	56.4	26.4	52.5	38.5	66.4	41.7	61.7	32.1	66.8	52.7	46.8	37.3	40.3	52.1	52.5	
BTF(FPFH)	42.0	54.6	34.4	54.6	32.2	50.9	66.8	51.0	49.0	60.9	69.9	40.1	63.3	61.8	52.2	52.0	58.6	58.6	61.0	71.9	
M3DM	57.7	53.7	57.4	63.7	54.1	63.4	66.3	68.4	61.7	46.4	40.9	30.9	50.1	55.7	42.3	77.7	63.9	53.9	55.6	62.7	
PatchCore(FPFH)	58.7	57.1	60.4	66.7	57.2	50.4	63.9	61.5	53.7	49.4	55.8	46.9	55.1	58.0	45.3	75.7	79.0	60.0	58.6	65.7	
PatchCore(PointMAE)	59.1	60.1	51.3	60.1	65.0	52.3	62.9	45.8	57.9	50.1	59.3	59.3	56.1	58.9	47.6	72.7	53.8	61.0	55.6	67.7	
CPMF	35.3	64.3	52.0	48.2	40.5	78.3	63.9	62.5	65.8	68.3	68.5	48.2	60.1	60.1	55.1	55.3	69.7	49.7	49.9	68.9	
Reg3D-AD	59.7	70.6	48.6	69.5	52.5	67.1	52.5	49.0	34.8	66.3	59.3	61.0	75.2	69.3	72.5	64.3	46.7	51.0	53.8	34.3	
IMRNet	67.1	66.0	55.2	70.0	64.0	68.1	70.2	68.5	59.9	67.6	<u>71.0</u>	58.0	<u>77.1</u>	73.7	<u>77.5</u>	65.2	65.2	64.3	<u>75.7</u>	54.8	
R3D-AD	<u>83.3</u>	<u>72.0</u>	<u>73.3</u>	<u>73.7</u>	<u>78.1</u>	<u>81.9</u>	<u>77.8</u>	<u>74.1</u>	<u>76.7</u>	<u>74.4</u>	65.6	<u>68.3</u>	75.6	<u>82.2</u>	73.0	68.1	<u>67.0</u>	<u>77.6</u>	<u>75.7</u>	89.0	
PO3AD	100.0	83.3	90.0	93.3	92.6	92.2	82.9	83.3	88.1	84.9	85.3	78.7	87.7	85.9	79.2	<u>67.0</u>	87.1	83.3	99.5		
<i>Unified Method</i>																					
MC3D-AD	<u>96.2</u>	<u>80.5</u>	<u>79.5</u>	<u>70.9</u>	<u>75.6</u>	<u>93.0</u>	97.8	<u>71.9</u>	<u>88.5</u>	<u>91.1</u>	<u>75.4</u>	<u>89.8</u>	<u>78.4</u>	<u>79.3</u>	<u>70.1</u>	<u>83.5</u>	<u>76.1</u>	<u>74.3</u>	<u>95.2</u>	77.6	
SeDiR (Ours)	97.6	88.6	92.9	91.6	98.4	95.9	<u>95.6</u>	92.6	96.7	98.5	97.9	91.1	93.3	98.5	98.9	99.6	87.4	99.5	100.0	<u>66.7</u>	
Method	headset0	headset1	helmet0	helmet1	helmet2	helmet3	jar	phone	shelf0	tap0	tap1	vase0	vase1	vase2	vase3	vase4	vase5	vase7	vase8	vase9	Mean
<i>Category-Specific Method</i>																					
BTF(Raw)	37.8	51.5	55.3	34.9	60.2	52.6	42.0	56.3	16.4	52.5	57.3	53.1	54.9	41.0	71.7	42.5	58.5	44.8	42.4	56.4	49.3
BTF(FPFH)	52.0	49.0	57.1	71.9	54.2	44.4	58.6	67.1	60.9	56.0	54.6	34.2	21.9	54.6	69.9	51.0	40.9	51.8	66.8	26.8	52.8
M3DM	57.7	61.7	52.6	42.7	62.3	37.4	56.4	35.7	56.4	75.4	73.9	57.4	42.7	73.7	43.9	47.6	43.9	65.7	66.3	66.3	55.2
PatchCore(FPFH)	58.3	63.7	54.6	48.4	42.5	40.4	49.4	38.8	49.4	<u>75.3</u>	<u>76.6</u>	60.4	42.3	72.1	44.9	50.6	44.9	69.3	66.2	66.0	56.8
PatchCore(PointMAE)	59.1	62.7	55.6	55.2	44.7	42.4	48.3	48.8	52.3	45.8	53.8	51.3	55.2	74.1	46.0	51.6	46.0	65.0	66.3	62.9	56.2
CPMF	64.3	45.8	55.5	58.9	46.2	52.0	61.0	50.9	68.5	35.9	69.7	58.2	34.5	58.2	58.2	51.4	58.2	39.7	52.9	60.9	55.9
Reg3D-AD	53.7	61.0	60.0	38.1	61.4	36.7	59.2	41.4	<u>68.8</u>	67.6	64.1	48.6	70.2	60.5	65.0	50.0	65.0	46.2	62.0	59.4	57.2
IMRNet	72.0	67.6	59.7	60.0	<u>64.1</u>	57.3	78.0	75.5	60.3	67.6	69.6	55.2	75.7	61.4	70.0	52.4	70.0	63.5	63.0	59.4	66.1
R3D-AD	<u>73.8</u>	<u>79.5</u>	<u>75.7</u>	<u>72.0</u>	<u>63.3</u>	<u>70.7</u>	<u>83.8</u>	<u>76.2</u>	69.6	73.6	90.0	<u>73.3</u>	72.9	<u>75.2</u>	<u>74.2</u>	<u>63.0</u>	<u>74.2</u>	<u>77.1</u>	<u>72.1</u>	<u>71.8</u>	<u>74.9</u>
PO3AD	80.8	92.3	76.2	96.1	86.9	75.4	86.6	77.6	57.3	74.5	68.1	85.8	<u>74.2</u>	95.2	82.1	67.5	85.2	96.6	73.9	83.0	83.9
<i>Unified Method</i>																					
MC3D-AD	86.2	88.6	<u>67.2</u>	100.0	60.9	97.9	97.1	91.9	84.1	94.5	97.0	<u>79.5</u>	<u>85.7</u>	<u>92.9</u>	76.1	<u>87.6</u>	76.1	93.8	67.0	73.6	<u>84.2</u>
SeDiR (Ours)	<u>84.9</u>	89.0	96.5	100.0	87.0	100.0	100.0	<u>90.5</u>	88.7	<u>92.7</u>	<u>89.3</u>	88.8	97.1	78.8	92.4	94.8	100.0	87.3	94.2	93.3	

Table 3. Comparison of mean point-level AUROC (%) on Real3D-AD and Anomaly-ShapeNet datasets. The detailed per-category results are provided in the supplementary.

Method	Real3D-AD	Anomaly-ShapeNet
<i>Category-Specific Method</i>		
BTF(Raw)	57.1	55.0
BTF(FPFH)	73.3	62.8
M3DM	62.0	61.6
PatchCore(FPFH)	68.2	58.0
PatchCore(PointMAE)	62.0	57.7
CPMF	<u>75.8</u>	57.3
IMRNet	–	65.0
Reg3D-AD	70.5	66.8
Group3AD	73.5	–
ISMP	83.6	<u>69.1</u>
PO3AD	65.0	89.8
<i>Unified Method</i>		
MC3D-AD	76.8	<u>75.8</u>
SeDiR (Ours)	80.6	81.0

ing multi-resolution geometric cues with an adaptive context token helps form a category-aware global representation. Adding C3L improves O-AUROC by 2–3%, as it reduces inter-category entanglement and yields more discriminative embeddings. Finally, GGD brings another 1–2%, showing that geometry-guided reconstruction encourages semantically consistent outputs. These results collectively validate that each component contributes complementarily and that the overall framework effectively realizes the idea of Semantically Disentangled Reconstruction.

Analysis of loss components in C3L. Tab. 5 analyzes

Table 4. Ablation studies on the effectiveness of core components.

CFG	C3L	GGD	O-AUROC (↑)	P-AUROC (↑)
			75.1	78.1
✓			76.4	78.4
✓	✓		79.2	79.0
✓	✓	✓	81.0	80.6

Table 5. Ablation studies on the contribution of each loss in C3L.

\mathcal{L}_{scl}	\mathcal{L}_{cls}	\mathcal{L}_{cos}	O-AUROC (↑)	P-AUROC (↑)
✓			79.1	78.8
✓	✓		80.0	79.3
✓	✓	✓	81.0	80.6

the effects of the three loss components in the C3L module—namely, the supervised contrastive loss (\mathcal{L}_{scl}), the auxiliary classification loss (\mathcal{L}_{cls}), and the multi-resolution cosine alignment loss (\mathcal{L}_{cos}). Using only \mathcal{L}_{scl} achieves reasonable performance, showing that contrastive learning alone provides meaningful feature separation. Adding \mathcal{L}_{cls} yields a slight improvement, confirming that explicit category supervision enhances semantic discrimination across object classes. Finally, adding \mathcal{L}_{cos} yields a further 1% gain, showing that cross-resolution consistency enhances representation stability. Overall, combining the three losses reinforces semantic disentanglement and preserves intra-category coherence, maximizing detection performance.

Geometry-Guided strategies in GGD. Tab. 6 compares different strategies for injecting geometric priors within the Geometry-Guided Decoder (GGD). Our bias-based design achieves the best performance, while masking (as in

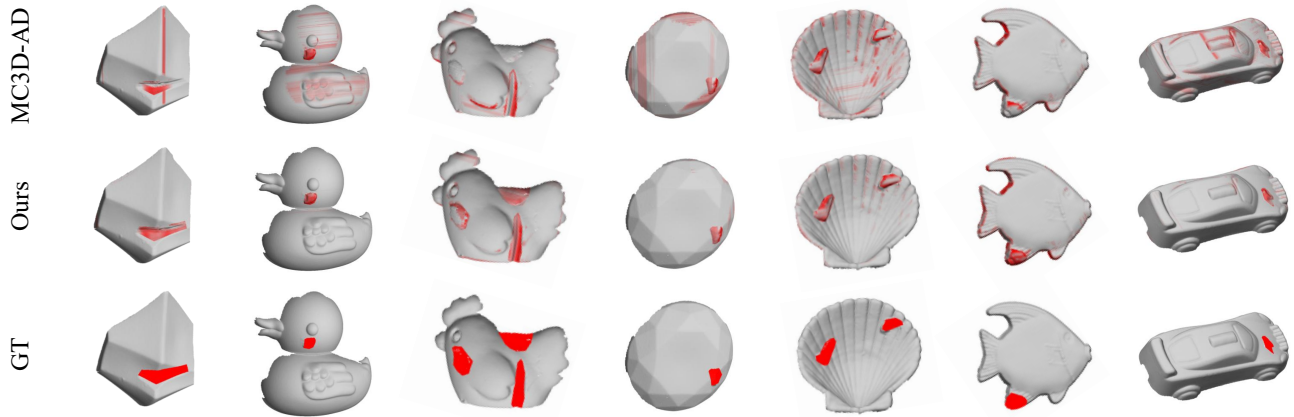


Figure 5. Qualitative comparison with MC3D-AD across various object categories in Real3D-AD dataset. Red colored regions indicate abnormalities (e.g., bulge, sink). MC3D-AD often misses true anomalies or yields false positives, whereas our method delivers more accurate and complete localization aligned with the ground truth.

Table 6. Comparison of different guidance strategies in GGD.

Method	O-AUROC (\uparrow)	P-AUROC (\uparrow)
Masking	79.8	79.6
Gating	79.7	78.9
Bias (Ours)	81.0	80.6

MC3D-AD) or gating geometric priors leads to lower performance. This indicates that incorporating geometric cues as an attention bias provides a more stable and fine-grained integration of spatial structure. This bias formulation more effectively enforces geometry-consistent reconstruction under category semantics, resulting in improved anomaly detection and localization.

Table 7. Comparison of different global token strategies.

Method	O-AUROC (\uparrow)	P-AUROC (\uparrow)
ACT	78.5	78.5
Max	76.4	75.5
Mean	78.2	78.7
CFG (Ours)	81.0	80.6

Comparison of global token configuration strategies.

Tab. 7 compares alternative strategies for constructing the global token in CFG. Replacing the fusion formulation in Eq. (5) with either the ACT alone or simple pooling operations (Max or Mean) leads to clear performance drops, showing that these variants fail to capture sufficient contextual and spatial information. In contrast, the proposed CFG achieves the highest O-AUROC and P-AUROC by integrating multi-resolution geometric features with the adaptive context, producing a richer and more discriminative global representation. These results demonstrate that CFG provides stronger semantic consistency and discriminability than conventional global summarization methods.

4.4. Qualitative Results

Fig. 5 shows qualitative comparisons between MC3D-AD and our method across various object categories in Real3D-AD. MC3D-AD often fails to accurately highlight the true anomalous regions, frequently missing some defective areas or producing false activations on normal surfaces. In contrast, the proposed method provides more precise localization of anomalies. This improvement suggests that incorporating semantic identity-aware representation learning and semantically guided reconstruction allows the model to better capture category-consistent semantics, leading to more reliable anomaly localization across diverse objects. Additional qualitative results are provided in the supplementary.

5. Conclusion

In this paper, we presented a unified framework for multi-category 3D anomaly detection, termed Semantically Disentangled Reconstruction (SeDiR). Unlike conventional unified models that reconstruct before understanding what is being reconstructed, our method first establishes a clear semantic identity and then performs reconstruction. By combining Coarse-to-Fine Global Tokenization, Category-Conditioned Contrastive Learning, and the Geometry-Guided Decoder, the method learns disentangled, category-aware representations and produces semantically aligned, geometrically consistent reconstructions. Extensive experiments show that each component provides complementary gains—CFG improves global semantic awareness, C3L enhances category separation, and GGD enforces geometry-consistent reconstruction—collectively achieving state-of-the-art results across multiple benchmarks. We believe these findings provide new insights into integrating semantic and geometric reasoning for robust 3D perception and open promising directions for cross-domain and open-set 3D anomaly detection.

Acknowledgments

This work was supported by the National Research Foundation of Korea (NRF) grant funded by the Korea government(MSIT)(RS-2024-00456589) and Korea Planning & Evaluation Institute of Industrial Technology(KEIT) grant funded by the Korea government(MOTIE) (No. RS2024-00442120, Development of AI technology capable of robustly recognizing abnormal and dangerous situations and behaviors during night and bad weather conditions).

References

- [1] Jimmy Lei Ba, Jamie Ryan Kiros, and Geoffrey E Hinton. Layer normalization. *arXiv preprint arXiv:1607.06450*, 2016. 4
- [2] Yunkang Cao, Xiaohao Xu, and Weiming Shen. Complementary pseudo multimodal feature for point cloud anomaly detection. *Pattern Recognition*, 156:110761, 2024. 6
- [3] Jiayi Cheng, Can Gao, Jie Zhou, Jiajun Wen, Tao Dai, and Jinbao Wang. Mc3d-ad: A unified geometry-aware reconstruction model for multi-category 3d anomaly detection. In *Proceedings of the Thirty-Fourth International Joint Conference on Artificial Intelligence, IJCAI-25*, pages 837–845. International Joint Conferences on Artificial Intelligence Organization, 2025. Main Track. 1, 2, 3, 6, 11
- [4] Thomas Defard, Aleksandr Setkov, Angelique Loesch, and Romaric Audigier. Padim: a patch distribution modeling framework for anomaly detection and localization. In *International conference on pattern recognition*, pages 475–489. Springer, 2021. 3
- [5] Lei Fan, Junjie Huang, Donglin Di, Anyang Su, Tianyou Song, Maurice Pagnucco, and Yang Song. Salvaging the overlooked: Leveraging class-aware contrastive learning for multi-class anomaly detection. In *Proceedings of the IEEE/CVF International Conference on Computer Vision*, pages 21419–21428, 2025. 3
- [6] Qingqing Fang, Qinliang Su, Wenxi Lv, Wenchao Xu, and Jianxing Yu. Boosting fine-grained visual anomaly detection with coarse-knowledge-aware adversarial learning. In *Proceedings of the AAAI Conference on Artificial Intelligence*, pages 16532–16540, 2025. 3
- [7] Matic Fučka, Vitjan Zavrtanik, and Danijel Skočaj. Transfusion—a transparency-based diffusion model for anomaly detection. In *European conference on computer vision*, pages 91–108. Springer, 2024. 3
- [8] Jia Guo, Shuai Lu, Weihang Zhang, Fang Chen, Huiqi Li, and Hongen Liao. Dinomaly: The less is more philosophy in multi-class unsupervised anomaly detection. In *Proceedings of the Computer Vision and Pattern Recognition Conference*, pages 20405–20415, 2025. 3
- [9] Haoyang He, Yuhu Bai, Jiangning Zhang, Qingdong He, Hongxu Chen, Zhenye Gan, Chengjie Wang, Xiangtai Li, Guanzhong Tian, and Lei Xie. Mambaad: Exploring state space models for multi-class unsupervised anomaly detection. *Advances in Neural Information Processing Systems*, 37:71162–71187, 2024. 3
- [10] Haoyang He, Jiangning Zhang, Hongxu Chen, Xuhai Chen, Zhishan Li, Xu Chen, Yabiao Wang, Chengjie Wang, and Lei Xie. A diffusion-based framework for multi-class anomaly detection. In *Proceedings of the AAAI conference on artificial intelligence*, pages 8472–8480, 2024. 3
- [11] Dan Hendrycks and Kevin Gimpel. Gaussian error linear units (gelus). *arXiv preprint arXiv:1606.08415*, 2016. 4
- [12] Eliahu Horwitz and Yedid Hoshen. Back to the feature: classical 3d features are (almost) all you need for 3d anomaly detection. In *Proceedings of the IEEE/CVF Conference on Computer Vision and Pattern Recognition*, pages 2968–2977, 2023. 6
- [13] Chaoqin Huang, Qinwei Xu, Yanfeng Wang, Yu Wang, and Ya Zhang. Self-supervised masking for unsupervised anomaly detection and localization. *IEEE Transactions on Multimedia*, 25:4426–4438, 2022. 3
- [14] Ehtesham Iqbal, Samee Ullah Khan, Sajid Javed, Brain Moyo, Yahya Zweiri, and Yusra Abdulrahman. Multi-scale feature reconstruction network for industrial anomaly detection. *Knowledge-Based Systems*, 305:112650, 2024. 3
- [15] Prannay Khosla, Piotr Teterwak, Chen Wang, Aaron Sarna, Yonglong Tian, Phillip Isola, Aaron Maschinot, Ce Liu, and Dilip Krishnan. Supervised contrastive learning. *Advances in neural information processing systems*, 33:18661–18673, 2020. 5
- [16] Wenqiao Li, Xiaohao Xu, Yao Gu, Bozhong Zheng, Shenghua Gao, and Yingna Wu. Towards scalable 3d anomaly detection and localization: A benchmark via 3d anomaly synthesis and a self-supervised learning network. In *Proceedings of the IEEE/CVF conference on computer vision and pattern recognition*, pages 22207–22216, 2024. 1, 3, 5, 6, 11
- [17] Hanzhe Liang, Guoyang Xie, Chengbin Hou, Bingshu Wang, Can Gao, and Jinbao Wang. Look inside for more: Internal spatial modality perception for 3d anomaly detection. In *Proceedings of the AAAI Conference on Artificial Intelligence*, pages 5146–5154, 2025. 3, 6, 11
- [18] Yufei Liang, Jiangning Zhang, Shiwei Zhao, Runze Wu, Yong Liu, and Shuwen Pan. Omni-frequency channel-selection representations for unsupervised anomaly detection. *IEEE Transactions on Image Processing*, 32:4327–4340, 2023. 3
- [19] Jiaqi Liu, Guoyang Xie, Ruitao Chen, Xinpeng Li, Jinbao Wang, Yong Liu, Chengjie Wang, and Feng Zheng. Real3d-ad: A dataset of point cloud anomaly detection. *Advances in Neural Information Processing Systems*, 36:30402–30415, 2023. 1, 3, 5, 6, 11
- [20] Tongkun Liu, Bing Li, Xiao Du, Bingke Jiang, Leqi Geng, Feiyang Wang, and Zhuo Zhao. Simple and effective frequency-aware image restoration for industrial visual anomaly detection. *Advanced Engineering Informatics*, 64:103064, 2025. 3
- [21] Ilya Loshchilov and Frank Hutter. Decoupled weight decay regularization. *arXiv preprint arXiv:1711.05101*, 2017. 11
- [22] Ruiying Lu, YuJie Wu, Long Tian, Dongsheng Wang, Bo Chen, Xiyang Liu, and Ruimin Hu. Hierarchical vector quantized transformer for multi-class unsupervised anomaly

- detection. *Advances in Neural Information Processing Systems*, 36:8487–8500, 2023. 3
- [23] Laurens van der Maaten and Geoffrey Hinton. Visualizing data using t-sne. *Journal of machine learning research*, 9 (Nov):2579–2605, 2008. 2, 13
- [24] Yatian Pang, Eng Hock Francis Tay, Li Yuan, and Zhenghua Chen. Masked autoencoders for 3d point cloud self-supervised learning. *World Scientific Annual Review of Artificial Intelligence*, 1:2440001, 2023. 4, 11
- [25] Jonathan Pirnay and Keng Chai. Inpainting transformer for anomaly detection. In *International Conference on Image Analysis and Processing*, pages 394–406. Springer, 2022. 3
- [26] Charles Ruizhongtai Qi, Li Yi, Hao Su, and Leonidas J Guibas. Pointnet++: Deep hierarchical feature learning on point sets in a metric space. *Advances in neural information processing systems*, 30, 2017. 4, 11
- [27] Nicolae-Cătălin Ristea, Neelu Madan, Radu Tudor Ionescu, Kamal Nasrollahi, Fahad Shahbaz Khan, Thomas B Moeslund, and Mubarak Shah. Self-supervised predictive convolutional attentive block for anomaly detection. In *Proceedings of the IEEE/CVF conference on computer vision and pattern recognition*, pages 13576–13586, 2022. 3
- [28] Karsten Roth, Latha Pemula, Joaquin Zepeda, Bernhard Schölkopf, Thomas Brox, and Peter Gehler. Towards total recall in industrial anomaly detection. In *Proceedings of the IEEE/CVF conference on computer vision and pattern recognition*, pages 14318–14328, 2022. 3, 6
- [29] Luc PJ Sträter, Mohammadreza Salehi, Efstratios Gavves, Cees GM Snoek, and Yuki M Asano. Generalad: Anomaly detection across domains by attending to distorted features. In *European Conference on Computer Vision*, pages 448–465. Springer, 2024. 3
- [30] Xian Tao, Xinyi Gong, Xin Zhang, Shaohua Yan, and Chandranath Adak. Deep learning for unsupervised anomaly localization in industrial images: A survey. *IEEE Transactions on Instrumentation and Measurement*, 71:1–21, 2022. 3
- [31] Fuyun Wang, Tong Zhang, Yuanzhi Wang, Yide Qiu, Xin Liu, Xu Guo, and Zhen Cui. Distribution prototype diffusion learning for open-set supervised anomaly detection. In *Proceedings of the Computer Vision and Pattern Recognition Conference*, pages 20416–20426, 2025. 3
- [32] Yue Wang, Jinlong Peng, Jiangning Zhang, Ran Yi, Yabiao Wang, and Chengjie Wang. Multimodal industrial anomaly detection via hybrid fusion. In *Proceedings of the IEEE/CVF conference on computer vision and pattern recognition*, pages 8032–8041, 2023. 6
- [33] Shun Wei, Jieliang Jiang, and Xiaolong Xu. Uninet: A contrastive learning-guided unified framework with feature selection for anomaly detection. In *Proceedings of the Computer Vision and Pattern Recognition Conference*, pages 9994–10003, 2025. 3
- [34] Julian Wyatt, Adam Leach, Sebastian M Schmon, and Chris G Willcocks. Anoddpm: Anomaly detection with denoising diffusion probabilistic models using simplex noise. In *Proceedings of the IEEE/CVF conference on computer vision and pattern recognition*, pages 650–656, 2022. 3
- [35] Xudong Yan, Huaidong Zhang, Xuemiao Xu, Xiaowei Hu, and Pheng-Ann Heng. Learning semantic context from normal samples for unsupervised anomaly detection. In *Proceedings of the AAAI conference on artificial intelligence*, pages 3110–3118, 2021. 3
- [36] Haiming Yao, Yunkang Cao, Wei Luo, Weihang Zhang, Wenyong Yu, and Weiming Shen. Prior normality prompt transformer for multiclass industrial image anomaly detection. *IEEE Transactions on Industrial Informatics*, 20(10): 11866–11876, 2024. 3
- [37] Hang Yao, Ming Liu, Zhicun Yin, Zifei Yan, Xiaopeng Hong, and Wangmeng Zuo. Glad: Towards better reconstruction with global and local adaptive diffusion models for unsupervised anomaly detection. In *European Conference on Computer Vision*, pages 1–17. Springer, 2024. 3
- [38] Xincheng Yao, Zixin Chen, Chao Gao, Guangtao Zhai, and Chongyang Zhang. Resad: A simple framework for class generalizable anomaly detection. *Advances in Neural Information Processing Systems*, 37:125287–125311, 2024. 3
- [39] Jianan Ye, Weiguang Zhao, Xi Yang, Guangliang Cheng, and Kaizhu Huang. Po3ad: Predicting point offsets toward better 3d point cloud anomaly detection. In *Proceedings of the Computer Vision and Pattern Recognition Conference*, pages 1353–1362, 2025. 6, 11
- [40] Jihun Yi and Sungroh Yoon. Patch svdd: Patch-level svdd for anomaly detection and segmentation. In *Proceedings of the Asian conference on computer vision*, 2020. 3
- [41] Zhiyuan You, Lei Cui, Yujun Shen, Kai Yang, Xin Lu, Yu Zheng, and Xinyi Le. A unified model for multi-class anomaly detection. *Advances in Neural Information Processing Systems*, 35:4571–4584, 2022. 3
- [42] Vitjan Zavrtanik, Matej Kristan, and Danijel Skočaj. Reconstruction by inpainting for visual anomaly detection. *Pattern Recognition*, 112:107706, 2021. 3
- [43] Hengshuang Zhao, Li Jiang, Jiaya Jia, Philip HS Torr, and Vladlen Koltun. Point transformer. In *Proceedings of the IEEE/CVF international conference on computer vision*, pages 16259–16268, 2021. 11
- [44] Ying Zhao. Omnia: A unified cnn framework for unsupervised anomaly localization. In *Proceedings of the IEEE/CVF Conference on Computer Vision and Pattern Recognition*, pages 3924–3933, 2023. 3
- [45] Zheyuan Zhou, Le Wang, Naiyu Fang, Zili Wang, Lemiao Qiu, and Shuyou Zhang. R3d-ad: Reconstruction via diffusion for 3d anomaly detection. In *European conference on computer vision*, pages 91–107. Springer, 2024. 1, 3, 6
- [46] Hongze Zhu, Guoyang Xie, Chengbin Hou, Tao Dai, Can Gao, Jinbao Wang, and Linlin Shen. Towards high-resolution 3d anomaly detection via group-level feature contrastive learning. In *Proceedings of the 32nd ACM International Conference on Multimedia*, pages 4680–4689, 2024. 1, 3, 6

A Semantically Disentangled Unified Model for Multi-category 3D Anomaly Detection

Supplementary Material

Contents

- A. Implementation Details
- B. Details of Geometry-Derived Bias
- C. More Quantitative Results
- D. More Ablation Studies
- E. More Qualitative Results
- F. Limitation

A. Implementation Details

Model setup. We adopt PointMAE [24], pretrained on ModelNet40 (8k), as the local feature extractor $E(\cdot)$. Each point cloud is partitioned into 1024 groups via FPS [26], and multi-resolution neighborhoods are formed with sizes $\{128, 256, 512\}$. Positional embeddings follow Point Transformer [43], where (x, y, z) coordinates are encoded by a two-layer MLP with ReLU. The shared transformer encoder in CFGT and the Geometry-Guided Decoder each contain 4 layers with 8 attention heads. Before entering the transformer encoder, feature jittering is applied with scale 20.0 and probability 1.0. The buffer in C3L is set to 64 entries.

Training and inference setup. We train the model using AdamW [21] with a base learning rate of 1×10^{-4} and a cosine annealing schedule. The batch size is 1 and training is performed for 1000 epochs. The loss weights in C3L are set to $\lambda_{\text{scl}} = 0.001$, $\lambda_{\text{cls}} = 0.001$, and $\lambda_{\text{cos}} = 0.01$. During inference, reconstruction discrepancies are smoothed with a 1D Gaussian filter with kernel size $k_g = 511$ and standard deviation $\sigma = 0.2$. All experiments are conducted with PyTorch 1.13.0 and CUDA 11.7 on a single NVIDIA GeForce RTX 3090 GPU.

B. Details of Geometry-Derived Bias

Given a point cloud $\mathbf{P} = \{\mathbf{p}_n\}_{n=1}^N$, Farthest Point Sampling [26] selects g group centers $\mathcal{S} = \{\mathbf{s}_i\}_{i=1}^g$. For each center \mathbf{s}_i , an adaptive radius r is estimated per instance, and its neighborhood is defined as $\mathcal{N}_i = \{\mathbf{p}_j \mid \|\mathbf{p}_j - \mathbf{s}_i\| \leq r\}$. **Normal and curvature estimation.** Let \mathbf{C}_i denote the covariance matrix of centered neighbors:

$$\mathbf{C}_i = \text{Cov}(\mathcal{N}_i - \text{mean}(\mathcal{N}_i)). \quad (14)$$

Eigen-decomposition produces eigenvalues $\lambda_0 \leq \lambda_1 \leq \lambda_2$ and associated eigenvectors $\mathbf{e}_0, \mathbf{e}_1, \mathbf{e}_2$. The surface normal and curvature at the group center \mathbf{s}_i are obtained as:

$$\mathbf{n}_i = \mathbf{e}_0, \quad \kappa_i = \frac{\lambda_0}{\lambda_0 + \lambda_1 + \lambda_2}. \quad (15)$$

Local geometric variations. Geometric irregularity is quantified through angular deviations of normals and curvature fluctuations within each neighborhood:

$$v_i^{\text{norm}} = \frac{1}{|\mathcal{N}_i|} \sum_{\mathbf{p}_j \in \mathcal{N}_i} \angle(\mathbf{n}_i, \mathbf{n}_j), \quad (16)$$

$$v_i^{\text{curv}} = \frac{1}{|\mathcal{N}_i|} \sum_{\mathbf{p}_j \in \mathcal{N}_i} |\kappa_i - \kappa_j|. \quad (17)$$

These two measures form a geometric descriptor:

$$\mathbf{v}_i = [v_i^{\text{norm}}, v_i^{\text{curv}}]. \quad (18)$$

After normalization, the descriptor is passed through a lightweight MLP to produce a scalar bias:

$$\mathbf{B}_{\text{geo}}(i) = \text{MLP}(\mathbf{v}_i). \quad (19)$$

The lightweight MLP is a two-layer MLP with ReLU.

C. More Quantitative Results

P-AUROC results. Tab. S9 and Tab. S10 present the full category-level results for Real3D-AD [19] and Anomaly-ShapeNet [16], respectively. While PO3AD [39] and ISMP [17] achieve strong performance on specific datasets—excelling on synthetic and real-world domains respectively—our method maintains consistently solid performance across both datasets under the unified multi-category setting. These results highlight the robustness and general applicability of our framework across diverse object categories and domains.

O-AUPR results on Anomaly-ShapeNet. We additionally report object-level AUPR on the Anomaly-ShapeNet dataset in Tab. S11. Our method achieves strong performance across categories, outperforming existing approaches. These results further confirm that the proposed semantically disentangled reconstruction contributes to reliable object-level anomaly detection under the unified multi-category setting.

Table S1. Comparison of computational cost.

Method	Parameters (M)	FLOPs (G)
MC3D-AD	34.16	439.21
Ours	33.25	508.25

Computational cost. Tab. S1 compares the computational efficiency of our method with MC3D-AD [3]. Our model

uses fewer parameters (33.25M vs. 34.16M), indicating a slightly lighter architecture. Although the FLOPs are higher (508.25 vs. 439.21), this overhead mainly stems from the additional global tokenization and geometric bias modules. Overall, the model achieves improved performance while maintaining comparable computational complexity.

D. More Ablation Studies

To better understand how each design choice contributes to our framework, we conduct extensive ablation studies across several key components on the Real3D-AD dataset. These experiments provide a comprehensive analysis of how each factor influences semantic disentanglement, reconstruction quality, and overall anomaly detection performance.

Table S2. Ablation studies on the CFGT and C3L losses.

CFGT	\mathcal{L}_{scl}	\mathcal{L}_{cos}	\mathcal{L}_{cls}	O-AUROC (\uparrow)	P-AUROC (\uparrow)
	✓			78.8	79.0
		✓		77.9	78.7
	✓	✓		80.5	78.6
✓	✓			80.0	79.1
✓		✓		79.1	78.8
✓			✓	79.3	79.6
✓	✓	✓		80.5	79.8
✓		✓	✓	80.1	79.9
✓	✓		✓	80.0	79.3
✓	✓	✓	✓	81.0	80.6

Ablation on the CFGT and C3L losses. Tab. S2 reports the effect of enabling Coarse-to-Fine Global Tokenization (CFGT) module and the individual loss terms in C3L. Without CFGT, no global token is formed; the model instead applies supervised contrastive learning to a globally averaged feature, resulting in reasonable yet suboptimal performance. Enabling CFGT introduces a unified global token derived from multi-resolution features, which substantially strengthens category-conditioned contrastive learning. Adding the cosine alignment and auxiliary classification terms further improves performance, with the full configuration achieving the highest O-AUROC and P-AUROC. These results suggest that explicitly constructing a global token and supervising it with all C3L objectives yields the most discriminative and semantically disentangled representation.

Table S3. Comparison of different coarse-to-fine neighborhood ratios.

Ratios	O-AUROC (\uparrow)	P-AUROC (\uparrow)
{k, 4k, k/4}	80.3	79.4
{k, 3k, k/3}	80.9	79.8
{k, 1.5k, 2k/3}	79.9	79.8
{k, 2k, k/2}	81.0	80.6

Impact of coarse–fine neighborhood ratios. Tab. S3 reports the performance of different neighborhood ratio configurations used in the CFGT. We evaluate several coarse–fine combinations based on the base resolution k , including $\{k, 4k, k/4\}$, $\{k, 3k, k/3\}$, $\{k, 1.5k, 2k/3\}$, and $\{k, 2k, k/2\}$. Among these settings, the configuration $\{k, 2k, k/2\}$ achieves the best results on both O-AUROC and P-AUROC. Across the evaluated ratios, settings with a more balanced fine–base–coarse distribution—such as $\{k, 2k, k/2\}$ —tend to show more stable performance. This observation indicates that the choice of multi-resolution neighborhood arrangement can influence the effectiveness of global representation learning within CFGT.

Table S4. Comparison of different base neighborhood sizes k .

Size	O-AUROC (\uparrow)	P-AUROC (\uparrow)
{256, 512, 1024}	77.5	78.5
{64, 128, 256}	79.9	79.6
{128, 256, 512}	81.0	80.6

Effect of neighborhood sizes. Tab. S4 evaluates different neighborhood sizes used in the CFGT module. Three configurations with various *base* sizes are compared, among which the setting with a *base size* of 256 ($\{128, 256, 512\}$) achieves the highest O-AUROC and P-AUROC. The results show that neighborhood size introduces performance gap: larger neighborhoods tend to smooth out fine geometric cues, whereas smaller ones may lack sufficient structural context. A base size of 256 provides the most balanced fine–base–coarse composition, enabling stable multi-resolution feature extraction and yielding the most reliable performance among the evaluated choices.

Table S5. Comparison of different numbers of groups.

N	O-AUROC (\uparrow)	P-AUROC (\uparrow)
512	75.7	77.4
2048	77.7	78.4
1024	81.0	80.6

Effect of the number of groups. Tab. S5 evaluates the impact of varying the number of groups used to partition the point cloud. Among the three tested settings—512, 1024, and 2048 groups—the configuration with 1024 groups yields the best performance. A clear performance gap emerges due to the trade-off in spatial granularity. Using too few groups (e.g., 512) produces large spatial regions, causing each token to aggregate overly coarse geometry and reducing sensitivity to fine anomalies. In contrast, using too many groups (e.g., 2048) results in highly fragmented neighborhoods that capture limited local structure and introduce noise, weakening multi-resolution feature extraction. The configuration with 1024 groups achieves a balanced decomposition, providing sufficient geometric detail while

maintaining stable local neighborhoods. This result highlights the importance of selecting an appropriate grouping resolution for robust multi-resolution representation learning.

Table S6. Comparison of different buffer sizes in C3L.

L	O-AUROC (\uparrow)	P-AUROC (\uparrow)
32	79.6	79.8
128	80.3	80.3
10,000	80.5	79.2
64	81.0	80.6

Effect of buffer size in C3L. Tab. S6 examines the influence of buffer size in C3L. Reducing the buffer from 64 to 32 slightly degrades both O-AUROC and P-AUROC, implying that too few contrastive samples hinder stable supervised contrastive learning. Increasing the buffer (e.g., to 128 or 10,000) yields performance similar to that of size 64, suggesting diminishing returns once a moderate number of samples is available; excessively large buffers may even introduce stale embeddings that are misaligned with the current representation space. Overall, a buffer size of 64 provides the best balance between stability and efficiency, yielding the highest performance among the evaluated configurations.

Table S7. Comparison of different loss weights in C3L.

λ_{scl}	λ_{cos}	λ_{cls}	O-AUROC (\uparrow)	P-AUROC (\uparrow)
0.01	0.001	0.01	79.3	79.6
0.001	0.01	0.01	78.6	78.3
0.001	0.001	0.1	77.0	78.9
0.001	0.001	0.01	81.0	80.6

Effect of loss weights in C3L. Tab. S7 examines the sensitivity of C3L to different loss-weight configurations, obtained by scaling each term by a factor of 10. Overweighting any single component disrupts the balance among the supervised contrastive, cosine alignment, and auxiliary classification losses, leading to noticeable drops in both O-AUROC and P-AUROC. The weights used in the main experiments ($\lambda_{\text{scl}}=0.001$, $\lambda_{\text{cos}}=0.001$, $\lambda_{\text{cls}}=0.01$) achieve the best performance, indicating that C3L benefits from a well-balanced combination of objectives.

Table S8. Category prediction accuracy with different global representations.

Method	Accuracy (%)
Mean	78.1
Max	77.3
ACT	97.3

Effect of ACT for category representation. We evaluate the effectiveness of the proposed Adaptive Context Token

(ACT) as a global summary of category information. After freezing the pretrained model, we train an additional category prediction head for 100 epochs using three different global representations: mean pooling, max pooling, and ACT. As shown in Tab. S8, ACT achieves substantially higher classification accuracy, indicating that it captures category-discriminative semantics far more effectively than conventional pooling-based global tokens. This validates the use of ACT as the primary representation for category-aware learning in our framework.

E. More Qualitative Results

Qualitative comparison with MC3D-AD on Anomaly-ShapeNet. Fig. S2 presents additional qualitative comparisons with MC3D-AD on the Anomaly-ShapeNet dataset. While MC3D-AD often yields incomplete or noisy anomaly responses, our method more distinctly highlights anomaly regions and produces more coherent anomaly maps. These results further verify the stability and effectiveness of our method across diverse geometric patterns.

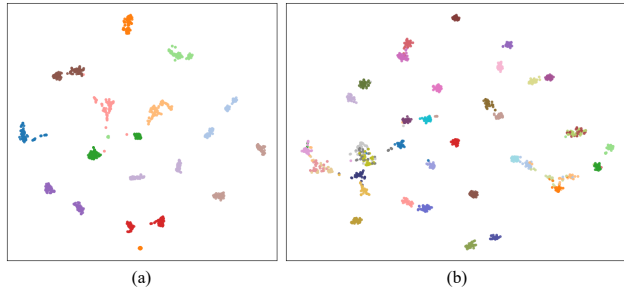


Figure S1. t-SNE visualization of the learned global tokens on (a) Real3D-AD (12 categories) and (b) Anomaly-ShapeNet (40 categories). The embeddings form well-structured clusters, indicating that the proposed method learns coherent and category-aware global representations across both datasets.

t-SNE visualization of global tokens. Figure S1 presents the t-SNE [23] embeddings of the global tokens learned on Real3D-AD and Anomaly-ShapeNet. Across both datasets, the embeddings exhibit well-formed clusters that reflect meaningful category structure, demonstrating that CFGT and C3L effectively promote category-aware global representations. The consistent clustering pattern, even as the number of categories increases, highlights the robustness of the proposed global tokenization strategy.

F. Limitation

While our model adopts a category-aware design, it does not outperform MC3D-AD on every category. This behavior is expected, as our framework is built for class-aware generalization rather than class-specific tuning. Instead of learning highly specialized representations for individual categories,

the model emphasizes semantic stability across categories, which inherently introduces trade-offs that may reduce performance in certain cases. Nevertheless, this design choice provides clear advantages in overall robustness and generalization. Analyzing the per-category AUROC variance reveals that MC3D-AD exhibits considerably larger fluctuations, whereas our method yields much lower variance and thus more uniform performance. On the Real3D-AD dataset, the O-AUROC variances of MC3D-AD and ours are 90.0 and 86.7, respectively; on the Anomaly-ShapeNet dataset, MC3D-AD reaches 102.9, while ours remains substantially lower at 43.4. These observations indicate that our approach is less sensitive to category-specific biases and achieves more stable reconstruction in the multi-category setting.

Table S9. Comparison of point-level AUROC (%) of various methods on the Real3D-AD dataset.

P-AUROC(↑)													
Method	Airplane	Car	Candybar	Chicken	Diamond	Duck	Fish	Gemstone	Seahorse	Shell	Starfish	Toffees	Mean
<i>Category-Specific Method</i>													
BTF(Raw)	56.4	64.7	73.5	60.9	56.3	60.1	51.4	59.7	52.0	48.9	39.2	62.3	57.1
BTF(FPFH)	<u>73.8</u>	70.8	<u>86.4</u>	73.5	<u>88.2</u>	<u>87.5</u>	70.9	<u>89.1</u>	51.2	57.1	50.1	81.5	73.3
M3DM	54.7	60.2	67.9	67.8	60.8	66.7	60.6	67.4	56.0	73.8	53.2	68.2	62.0
PatchCore(FPFH)	56.2	<u>75.4</u>	78.0	42.9	82.8	26.4	82.9	91.0	73.9	73.9	60.6	74.7	68.2
PatchCore(PointMAE)	56.9	60.9	62.7	72.9	71.8	52.8	71.7	44.4	63.3	70.9	58.0	58.0	62.0
CPMF	61.8	83.6	73.4	55.9	75.3	71.9	98.8	44.9	96.2	72.5	80.0	95.9	<u>75.8</u>
Reg3D-AD	63.1	71.8	72.4	67.6	83.5	50.3	82.6	54.5	81.7	<u>81.1</u>	61.7	75.9	70.5
Group3AD	63.6	74.5	73.8	<u>75.9</u>	86.2	63.1	83.6	56.4	<u>82.7</u>	79.8	62.5	80.3	73.5
ISMP	75.3	83.6	90.7	79.8	92.6	87.6	<u>88.6</u>	85.7	81.3	83.9	64.1	<u>89.5</u>	83.6
PO3AD	71.5	57.4	76.3	56.3	61.4	64.4	87.7	53.0	58.5	54.2	<u>65.9</u>	72.9	65.0
<i>Unified Method</i>													
MC3D-AD	<u>62.8</u>	<u>81.9</u>	<u>91.0</u>	64.0	<u>94.2</u>	<u>82.2</u>	<u>93.2</u>	<u>45.8</u>	<u>65.9</u>	<u>77.8</u>	<u>69.0</u>	<u>93.4</u>	<u>76.8</u>
Ours	66.6	90.8	95.1	<u>63.2</u>	97.7	83.4	96.7	54.7	73.9	79.8	70.9	94.0	80.6

Table S10. Comparison of point-level AUROC (%) of various methods on the Anomaly-ShapeNet dataset.

P-AUROC(↑)															
Method	ashtray0	bag0	bottle0	bottle1	bottle3	bow10	bow11	bow12	bow13	bow14	bow15	bucket0	bucket1		
<i>Category-Specific Method</i>															
BTF(Raw)	51.2	43.0	55.1	49.1	<u>72.0</u>	52.4	46.4	42.6	<u>68.5</u>	56.3	51.7	61.7	68.6		
BTF(FPFH)	62.4	<u>74.6</u>	64.1	54.9	62.2	71.0	<u>76.8</u>	51.8	59.0	67.9	69.9	40.1	63.3		
M3DM	57.7	63.7	66.3	63.7	53.2	65.8	66.3	<u>69.4</u>	65.7	62.4	48.9	<u>69.8</u>	69.9		
PatchCore(FPFH)	59.7	57.4	65.4	68.7	51.2	52.4	53.1	<u>62.5</u>	32.7	72.0	35.8	45.9	57.1		
PatchCore(PointMAE)	49.5	67.4	55.3	60.6	65.3	52.7	52.4	51.5	58.1	50.1	56.2	58.6	57.4		
CPMF	61.5	65.5	52.1	57.1	43.5	74.5	48.8	63.5	64.1	68.3	68.4	48.6	60.1		
Reg3D-AD	<u>69.8</u>	71.5	<u>88.6</u>	69.6	52.5	77.5	61.5	59.3	65.4	<u>80.0</u>	69.1	61.9	75.2		
IMRNet	67.1	66.8	55.6	<u>70.2</u>	64.1	<u>78.1</u>	70.5	68.4	59.9	57.6	<u>71.5</u>	58.5	<u>77.4</u>		
PO3AD	96.2	94.9	91.2	84.4	88.0	97.8	91.4	91.8	93.5	96.7	94.1	75.5	89.9		
<i>Unified Method</i>															
MC3D-AD	80.1	<u>81.5</u>	<u>89.5</u>	<u>88.3</u>	<u>90.1</u>	<u>82.7</u>	<u>53.4</u>	<u>60.7</u>	<u>78.3</u>	<u>65.4</u>	<u>55.2</u>	79.0	89.5		
Ours	<u>76.4</u>	89.8	91.1	89.8	94.5	86.6	70.0	79.5	86.9	80.6	64.6	<u>71.7</u>	<u>88.4</u>		
Method	cap0	cap3	cap4	cap5	cup0	cup1	eraser0	headset0	headset1	helmet0	helmet1	helmet2	helmet3		
<i>Category-Specific Method</i>															
BTF(Raw)	52.4	68.7	46.9	37.3	63.2	56.1	63.7	57.8	47.5	50.4	44.9	60.5	70.0		
BTF(FPFH)	<u>73.0</u>	65.8	52.4	58.6	<u>79.0</u>	61.9	71.9	62.0	59.1	57.5	<u>74.9</u>	64.3	72.4		
M3DM	53.1	60.5	71.8	65.5	71.5	55.6	71.0	58.1	58.5	59.9	<u>42.7</u>	62.3	65.5		
PatchCore(FPFH)	47.2	65.3	59.5	<u>79.5</u>	65.5	59.6	<u>81.0</u>	58.3	46.4	54.8	48.9	45.5	<u>73.7</u>		
PatchCore(PointMAE)	54.4	48.8	72.5	54.5	51.0	<u>85.6</u>	37.8	57.5	42.3	58.0	56.2	65.1	61.5		
CPMF	60.1	55.1	55.3	55.1	49.7	50.9	68.9	69.9	45.8	55.5	54.2	51.5	52.0		
Reg3D-AD	63.2	<u>71.8</u>	<u>81.5</u>	46.7	68.5	69.8	75.5	58.0	<u>62.6</u>	<u>60.0</u>	62.4	<u>82.5</u>	62.0		
IMRNet	71.5	70.6	75.3	74.2	64.3	68.8	54.8	<u>70.5</u>	47.6	59.8	60.4	64.4	66.3		
PO3AD	95.7	94.8	94.0	86.4	90.9	93.2	97.4	82.3	90.7	87.8	94.8	93.2	84.6		
<i>Unified Method</i>															
MC3D-AD	<u>86.7</u>	<u>92.2</u>	<u>88.0</u>	<u>88.5</u>	<u>82.9</u>	<u>71.5</u>	85.6	<u>66.6</u>	70.9	<u>74.4</u>	<u>58.2</u>	<u>81.7</u>	<u>60.2</u>		
Ours	90.0	97.2	94.0	95.0	87.1	84.2	<u>74.8</u>	70.8	<u>68.7</u>	81.0	59.6	88.5	70.1		
Method	jar	phone	shelf0	tap0	tap1	vase0	vase1	vase2	vase3	vase4	vase5	vase7	vase8	vase9	Mean
<i>Category-Specific Method</i>															
BTF(Raw)	42.3	58.3	46.4	52.7	56.4	61.8	54.9	40.3	60.2	61.3	58.5	57.8	55.0	56.4	55.0
BTF(FPFH)	42.7	67.5	61.9	56.8	59.6	64.2	61.9	64.6	<u>69.9</u>	71.0	42.9	54.0	66.2	56.8	62.8
M3DM	54.1	35.8	55.4	65.4	71.2	60.8	60.2	73.7	65.8	65.5	64.2	51.7	55.1	66.3	61.6
PatchCore(FPFH)	47.8	48.8	61.3	73.3	76.8	65.5	45.3	72.1	43.0	50.5	44.7	69.3	57.5	66.3	58.0
PatchCore(PointMAE)	48.7	88.6	54.3	85.8	54.1	<u>67.7</u>	55.1	<u>74.2</u>	46.5	52.3	57.2	65.1	36.4	42.3	57.7
CPMF	61.1	54.5	78.3	45.8	65.7	45.8	48.6	58.2	58.2	51.4	65.1	50.4	52.9	54.5	57.3
Reg3D-AD	59.9	59.9	<u>68.8</u>	58.9	<u>74.1</u>	54.8	60.2	40.5	51.1	<u>75.5</u>	62.4	<u>88.1</u>	<u>81.1</u>	<u>69.4</u>	<u>66.8</u>
IMRNet	<u>76.5</u>	74.2	60.5	68.1	69.9	53.5	<u>68.5</u>	61.4	40.1	52.4	<u>68.2</u>	59.3	63.5	69.1	65.0
PO3AD	87.1	<u>81.0</u>	66.3	<u>78.3</u>	69.2	95.5	88.2	97.8	88.4	90.2	93.7	98.2	95.0	95.2	89.8
<i>Unified Method</i>															
MC3D-AD	<u>84.8</u>	<u>85.4</u>	<u>65.8</u>	<u>52.4</u>	<u>53.7</u>	87.0	72.6	<u>82.2</u>	<u>79.7</u>	<u>78.6</u>	<u>64.7</u>	<u>61.6</u>	<u>88.5</u>	<u>77.6</u>	<u>75.9</u>
Ours	91.1	89.1	67.9	59.7	63.0	<u>84.6</u>	<u>72.2</u>	85.0	83.0	88.4	76.6	77.7	90.0	83.5	81.0

Table S11. Comparison of object-level AUPR (%) of various methods on the Anomaly-ShapeNet dataset.

O-AUPR(↑)															
Method	ashtray0	bag0	bottle0	bottle1	bottle3	bow10	bow11	bow12	bow13	bow14	bow15	bucket0	bucket1		
<i>Category-Specific Method</i>															
BTF(Raw)	57.8	45.8	46.6	57.3	54.3	58.8	46.4	57.6	<u>65.4</u>	60.1	61.5	65.2	62.0		
BTF(FPFH)	65.1	55.1	64.4	62.5	60.2	57.6	<u>64.8</u>	51.5	49.9	63.2	<u>69.9</u>	48.3	64.8		
M3DM	63.2	64.2	<u>76.3</u>	67.4	45.1	52.5	51.5	63.0	63.5	57.1	60.1	60.9	50.7		
PatchCore(FPFH)	44.5	60.8	61.5	67.7	57.9	54.8	54.5	61.1	62.0	57.5	54.1	60.4	56.5		
PatchCore(PointMAE)	<u>67.9</u>	60.1	54.5	64.5	<u>65.1</u>	56.2	61.1	45.6	55.6	60.1	58.5	54.1	64.2		
CPMF	45.3	65.5	58.8	59.2	50.5	<u>77.5</u>	62.1	60.1	41.8	<u>68.3</u>	68.5	<u>66.2</u>	50.1		
Reg3D-AD	58.8	60.8	63.2	69.5	47.4	49.4	51.5	49.5	44.1	62.4	55.5	63.2	71.4		
IMRNet	61.2	<u>66.5</u>	55.8	<u>70.2</u>	64.8	48.1	50.4	<u>68.1</u>	61.4	63.0	65.2	57.8	<u>73.2</u>		
PO3AD	99.9	80.9	92.7	95.9	96.2	94.6	90.5	88.8	92.7	98.5	90.4	92.3	88.2		
<i>Unified Method</i>															
Ours	97.5	88.0	93.4	94.3	99.0	97.5	96.1	93.6	97.0	98.9	98.5	94.1	94.4		
Method	cap0	cap3	cap4	cap5	cup0	cup1	eraser0	headset0	headset1	helmet0	helmet1	helmet2	helmet3		
<i>Category-Specific Method</i>															
BTF(Raw)	65.9	61.2	51.5	65.3	60.1	70.1	42.5	37.9	51.5	55.9	38.8	61.5	52.6		
BTF(FPFH)	61.8	57.9	54.5	59.3	58.5	65.1	71.9	53.1	52.3	56.8	<u>72.1</u>	58.8	56.4		
M3DM	56.4	65.2	47.7	64.2	57.0	<u>75.2</u>	62.5	63.2	62.3	52.8	62.7	<u>63.6</u>	45.8		
PatchCore(FPFH)	58.5	45.7	65.5	72.5	60.4	58.6	58.4	<u>70.1</u>	60.1	52.5	63.0	47.5	49.4		
PatchCore(PointMAE)	56.1	58.3	<u>72.1</u>	54.2	64.2	71.0	<u>80.1</u>	51.5	42.3	63.3	57.1	49.6	61.1		
CPMF	60.1	54.1	64.5	69.7	<u>64.7</u>	60.9	54.4	60.2	61.9	33.3	50.1	47.7	<u>64.5</u>		
Reg3D-AD	69.3	<u>71.1</u>	62.3	<u>77.0</u>	53.1	63.8	42.4	53.8	61.7	60.0	38.1	61.8	46.8		
IMRNet	<u>71.1</u>	70.2	65.8	50.2	45.5	62.7	59.9	<u>70.1</u>	<u>65.6</u>	<u>69.7</u>	61.5	60.2	57.5		
PO3AD	84.1	90.6	87.6	80.1	87.9	87.0	99.5	76.5	91.4	86.4	96.1	93.4	84.9		
<i>Unified Method</i>															
Ours	98.8	99.2	99.7	87.5	99.5	100.0	57.8	86.9	89.9	97.9	100.0	89.4	100.0		
Method	jar	phone	shelf0	tap0	tap1	vase0	vase1	vase2	vase3	vase4	vase5	vase7	vase8	vase9	Mean
<i>Category-Specific Method</i>															
BTF(Raw)	42.8	61.3	62.4	53.5	59.4	56.2	44.1	41.3	<u>71.7</u>	42.8	61.5	54.7	41.6	48.2	54.9
BTF(FPFH)	47.9	<u>66.2</u>	61.1	61.0	57.5	64.1	65.5	56.9	65.2	58.7	47.2	59.2	62.4	63.8	59.8
M3DM	55.5	46.4	66.5	<u>72.2</u>	63.8	78.8	65.2	61.5	55.1	52.6	63.3	64.8	46.3	65.1	60.3
PatchCore(FPFH)	49.9	33.2	50.4	71.2	68.4	64.5	62.3	<u>80.1</u>	48.1	<u>77.7</u>	51.5	62.1	51.5	<u>66.0</u>	58.8
PatchCore(PointMAE)	46.3	65.2	54.3	71.2	54.2	54.8	57.2	71.1	45.5	58.6	58.5	<u>65.2</u>	65.5	63.4	59.5
CPMF	61.8	65.5	68.1	63.9	69.7	63.2	64.5	63.2	58.8	65.5	51.8	43.2	<u>67.3</u>	61.8	59.7
Reg3D-AD	60.1	61.4	67.5	67.6	59.9	61.5	46.8	64.1	65.1	50.5	58.8	45.5	62.9	57.4	58.4
IMRNet	<u>76.0</u>	55.2	62.5	40.1	79.6	57.3	<u>72.5</u>	65.5	70.8	52.8	<u>65.4</u>	60.1	63.9	46.2	<u>62.1</u>
PO3AD	91.5	80.3	<u>68.0</u>	85.6	<u>70.9</u>	<u>75.3</u>	78.9	96.3	90.2	82.4	87.9	97.1	83.3	90.4	88.1
<i>Unified Method</i>															
Ours	100.0	88.8	91.7	93.9	82.6	87.6	97.4	97.5	84.7	95.3	94.8	100.0	91.0	96.4	93.8

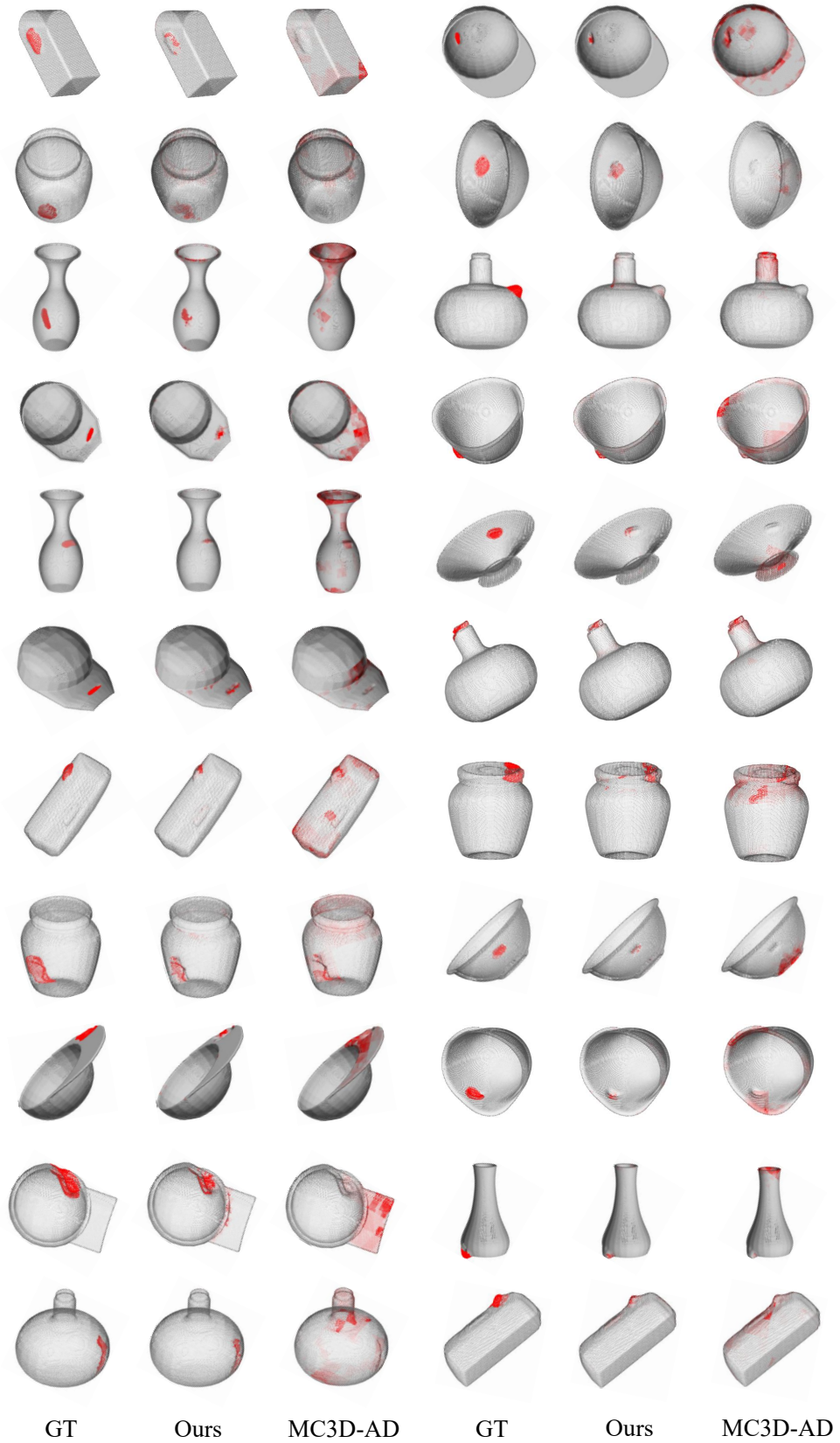


Figure S2. Additional qualitative comparison with MC3D-AD on the Anomaly-ShapeNet dataset.